Experiments in Fluids (2023) 64:148
https://doi.org/10.1007/s00348-023-03688-7

RESEARCH ARTICLE

LIF-based quantification of the species transport during droplet impact onto thin liquid films

Species transport during droplet impact onto thin liquid films

Hatim Ennayar[1] · Philipp Brockmann[1] · Jeanette Hussong[1]

Received: 22 May 2023 / Revised: 24 July 2023 / Accepted: 26 July 2023 / Published online: 17 August 2023

Abstract

In the present study, laser-induced fluorescence (LIF) is used to investigate the mixing process of a droplet impacting onto a thin liquid film. A robust multidimensional calibration procedure is developed enabling the extraction of local instantaneous dye concentrations as well as film heights. A series of validation measurements are conducted confirming a low reconstruction error of 4.53%. The impact-induced mixing process is thoroughly investigated across various liquid film thicknesses to examine the propagation of the mixing zone and the instantaneous radial concentration gradients within it. It is shown that the maximum extent of the mixing zone scales inversely proportional with the thickness of the liquid film. Within our experiments, we discover the formation of wall-induced vortex ring instabilities subsequent to impact. The disintegration of vortex rings during droplet impact significantly enhances convection-driven mixing, as quantified by the coefficient of variation.

Graphical abstract

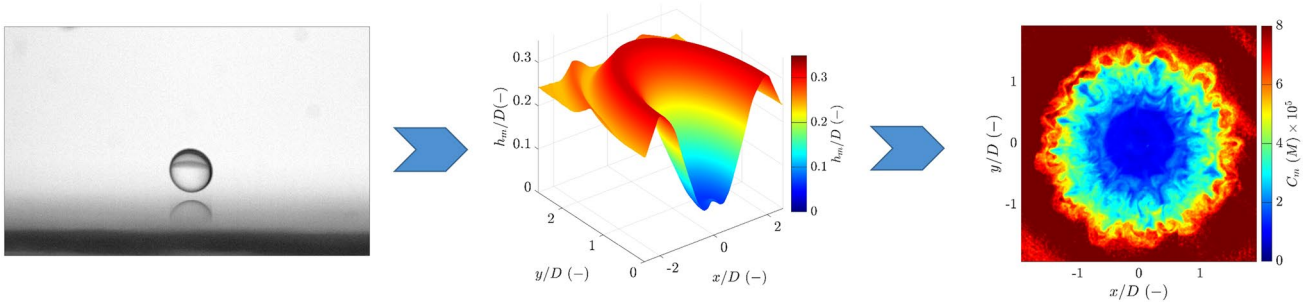

1 Introduction

Droplet impact dynamics has always been of great interests in various fields, whether the impact is onto a solid substrate, a thin liquid film or a deep pool. Due to its large occurrence in natural and industrial environments, understanding the principle physics of droplet impingement is of high interest in fundamental research as well as in technical applications, such as spray coating and fuel injection. The impact mechanism has been intensively investigated throughout last decades. Key parameters influencing the outcome of droplet impacts are thoroughly reviewed in (Yarin et al. 2006; Josserand and Thoroddsen 2016, and Breitenbach et al. 2018). During impact, the dynamics of a droplet with diameter D and velocity U is governed by the Reynolds $\mathrm{Re} = \frac{UD}{\nu}$ and Weber $\mathrm{We} = \frac{\rho D U^2}{\sigma}$ numbers, where ν, ρ and σ represent the kinematic viscosity, density and surface tension of the droplet.

In the case of droplet impacts onto liquid films, which is the focus of this paper, the film thickness h also contributes in the final outcome and another dimensionless number,

✉ Hatim Ennayar
ennayar@sla.tu-darmstadt.de

[1] Institute for Fluid Mechanics and Aerodynamics, TU Darmstadt, Flughafenstr. 19, 64347 Darmstadt-Griesheim, Germany

$\delta = \frac{h}{D}$, has to be considered. Cossali et al. (1997) defined thin liquid films as those where δ lower than 1, whereas Tropea and Marengo (1999) included also thicknesses up to $\delta < 1.5$. In contrast to the deep pool regime where the droplet impact is independent of the liquid film thickness, in the thin film regime, the outcome of a droplet impact is highly sensitive to the film thickness. If δ decreases even further below 0.1, a new film regime is entered in which the impact outcome is dominated by wall features takes over (Wang and Chen 2000; Geppert 2019). This regime is called very thin film regime and will be also investigated in the present study.

The impact outcome can be classified in four regimes, depending on the magnitude of the impact energy as well as the film regime. The first outcome, which occurs at We numbers in the order of unity, is floating regime (Klyuzhin et al. 2010). The second one is bouncing and can be obtained also at low We as shown by Pan and Law (2007). These two impact regimes are mainly driven by surface tension forces. At larger We, the droplet penetrates into the film thereby creating an expanding crater and droplet-film coalescence. Depending on the impact energy, an impact outcome with either deposition or crown formation without splashing can be obtained (Rioboo et al. 2003). During long crown expansion times the crown rim can become unstable, break up and splash which is the last impact outcome referred as the splashing regime (Roisman et al. 2006). Mundo et al. (1995) introduced a dimensionless parameter $K = \mathrm{We}^{\frac{1}{2}}\mathrm{Re}^{\frac{1}{4}}$ for predicting splashing. Hereafter, various studies (Cossali et al. 1997; Wal et al. 2006) were dedicated to identify the critical K number that separates the splashing and no splashing regimes.

Due to its high complexity, studies of droplet impact on thin films address different phenomenological properties. Studies of Roisman et al. (2008), Berberović et al. (2009), Van Hinsberg et al. (2010) and Hann et al. (2016) focus on the expansion of the liquid crater during droplet impact, whereas other studies tend toward crown evolution and its break up into secondary droplets (e.g., Tropea and Roisman 2000; Roisman and Tropea 2002; Okawa et al. 2006; Thoroddsen et al. 2012; Kittel et al. 2018). In addition to the diverse range of phenomenological properties studied, the complexity of droplet impact on thin films is further compounded by the challenges associated with the generation of thin fluid films of precise thickness (Kurniawan et al. 2022).

Recently, the area of droplet-film mixing started drawing more attention. Here, the miscibility of the droplet and film liquids, which depends on factors such as the chemical properties, molecular structure, and intermolecular forces (Israelachvili 2011), plays a crucial role since it determines whether the two liquids will mix or not. In the case of immiscible liquids, an interface separating film and droplet is formed and the interfacial tension plays an important role in determining the outcome of the impact. In fact, for the impact of immiscible liquids, different impact regimes occur as described above. Lhuissier et al. (2013), for example, studied the impact of immiscible droplets onto on a deep pool and observed the fragmentation of the drop starting at a critical impact velocity. Shaikh et al. (2018), on the other hand, focused on the impact of immiscible droplets onto thin liquid films, and how the mean diameter of the fragments increases with the droplet Weber number.

In contrast to immiscible liquids, the impact of miscible droplets results in mixing governed by different mechanisms. The recent study of Ersoy and Eslamian (2019) describes six possible mixing mechanisms during droplet impact on thin film. These mechanisms include mixing due to the expansion and receding crater, the collapse of the crown on the film, finger formation, secondary droplets, surface waves resulting from the impact and finally diffusion. Furthermore, Khan et al. (2020) observed how lateral vibrations that lead to wavy films enhance the mixing during droplet impact in comparison with static films. In regard to the miscibility effect on the impact outcome, the observations of Chen et al. (2017) show that the formation of a crown and splashing are suppressed due to the enhancement of the kinetic energy transfer between the droplet and the film. Additionally, the receding morphology during the impact also gets affected when the two liquids (droplet/film) are miscible (Chen et al. 2017). Mixing of different miscible liquids during impact can be also be enhanced through Marangoni forces, where surface tension gradients lead to droplet spreading and mixing (Kim et al. 2015, 2017).

In some technical applications, such as fuel injection, as well as for gaining a deeper understanding of the mixing outcome it is important to quantify the mixing process during the early stages of impact, where inertial effects play a major role. Using a thermal tracing method, Li et al. (2017) determined the temperature distribution within a film during the impact of a cold droplet which can be correlated with the mixing ratio between two liquids, under the assumption that thermal and species diffusion coefficients are comparable. Moreover, both Ersoy and Eslamian (2019) and Khan et al. (2020) estimated the mixing efficiency of a dyed droplet impacting a thin film by evaluating the color intensity signal from grayscale images, where areas with intensities smaller than a certain threshold are considered mixed areas.

While preceding studies focused on determining the surface area percentage of the liquid film tinted by the dyed droplet, the radial evolution of species distribution during droplet impact has not been quantified up to date. Extracting these information is the key for understanding the mixing behavior, which is crucial for better predicting processes in various applications. For instance, inside downsized combustion engines, where high interactions between droplets and thin wall films exist (Maliha et al. 2022), understanding

the mixing phenomena is essential for optimizing combustion efficiency and reducing emissions. Therefore, the main goal of the present work is to establish a measurement technique that is able to provide spatially and temporally resolved species concentrations during the impact of a droplet onto a thin liquid film.

A common and well-suited technique for investigating the concentration distribution in thin films is based on laser-induced fluorescence (LIF). Since its first quantitative application by Owen (1976) for measuring instantaneous velocity and concentration in turbulent mixing flows, it has been applied by various authors Koochesfahani and Dimotakis (1985), Walker (1987), Arcoumanis et al. (1990). The principles of LIF are well described by Haugland (1996) and others (Andresen and Strube 1994; Demtröder 2014).

In the last decades, LIF has been applied and developed further for investigating the mixing phenomena in various applications. For instance, the mixing due to internal waves in oceans was investigated by Dossmann et al. (2016) in a laboratory scale, using planar LIF to extract density fields. Another recent study used LIF for extracting concentration distributions of the Rhodamine B dye in water to investigate the mixing process inside an annular coolant system (Li et al. 2019). While the previous studies used light sheet illumination, the present work employs a volume illumination. This enables the investigation of the species distribution throughout the entire liquid film depth.

LIF is also utilized to determine the local thickness variation of the liquid film during the impact. This feature is of great importance since not only the concentration of the fluorescent dye but also the thickness of the film are variables influencing the intensity of the emitted fluorescence signal during a droplet impact. In fact, many studies employed LIF to reconstruct liquid film thicknesses in various applications. Due to its non-intrusive characteristics, LIF is used to determine the fuel film thicknesses inside combustion engines (Alonso et al. 2010; Schulz et al. 2016). In addition, it has also been applied for thickness measurements in droplet impact scenarios. For instance, the work of Oldenziel et al. (2012) focused on the determination of the film thickness between a droplet and a two-fluid interface during coalescence. Also, in the recent work of Hann et al. (2016), droplet impact-induced profile variations of liquid thin films with dimensionless thickness δ ranging between 0.43 and 1.29 were investigated utilizing LIF.

In the present study, LIF is used to reconstruct the water film thickness during droplet impact with high spacial resolution for film thicknesses ranging between $\delta = 0.09$ and $\delta = 0.36$. Afterward, using the thickness data, instantaneous concentration distributions during the impact process are determined. Measurement accuracy and sensitivity are carefully evaluated and first insights into the species transport are presented.

2 Experimental setup

The experimental configuration for investigating the mixing of droplets upon impact onto thin liquid films by means of LIF consists of three principal parts. These include a drop generator, an impact substrate and the optical system. The drop generator system contains a 5 mL syringe (Braun GmbH) driven by a syringe pump as shown in Fig. 1. The syringe is connected via a tube with a blunt needle (Braun GmbH), which is mounted on an automatically controlled traverse allowing different drop heights. A constant flow rate is chosen to generate repeatable water droplets of diameter $D = 2.225 \pm 0.025$ mm.

The impact substrate is a 50 mm×50 mm glass substrate (Sigma-Aldrich). To increase its surface energy for a better adhesion of liquid films, the substrate is washed with water and detergent then submerged in an ultrasonic bath of isopropanol before use. Deionized water labeled with a fluorescent dye is then spread across the substrate. After pinning the film contact lines to the substrates edges, small amounts of the liquid are either added or taken from the film using a syringe to obtain the desired liquid film thickness. The initial film thickness is measured during this process by a chromatic-confocal point sensor (confocalDT IFS2407−0.8, Micro-epsilon, short: CPS) with an accuracy of ± 0.4 µm. The sensor is mounted on an automated arm granting a 3D displacement to the sensor in order to scan the overall

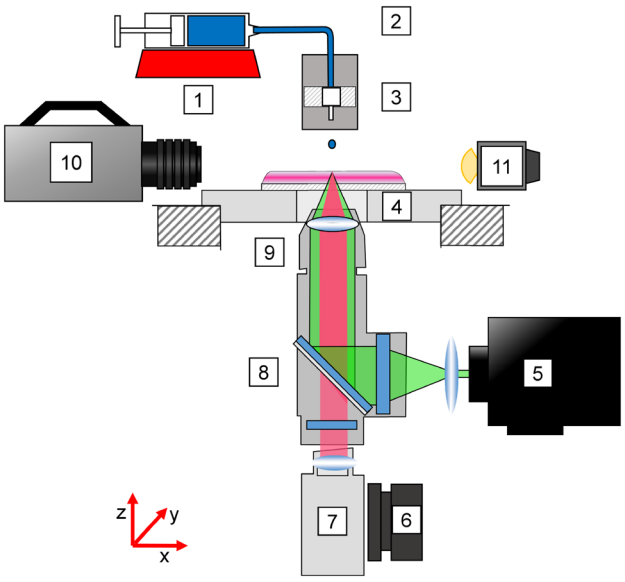

Fig. 1 Sketch of setup: (1) Syringe pump, (2) z-Traverse, (3) Cannula, (4) Thin liquid film on FTO glass substrate, (5) High power LED, (6) *x*,*y*,*z*-Traverse, (7) HS-Camera, (8) Dichroic mirror with bandpass filters, (9) Microscope Objective, (10) HS-Camera, (11) LED

film thickness. Three different film thicknesses are selected as listed in Table 1 together with other initial parameters.

The experiments are observed from two perspectives: a bottom view to extract the profile and the concentration variation during the impact, and a side view to determine the size and the velocity of the droplet. Moreover, coupling both side and bottom views offers a better understanding of the impact mechanisms. The bottom view apparatus consists of a custom-built microscope based on an optical tube (InfiniTube Special, Infinity Photo-Optical) illuminated with a 7 W high-power green chipped ($\lambda \approx 532$ nm) LED (ILA iLA.LPS v3). A dichroic mirror plus two band-pass filters, mounted on a filter cube (Thorlabs DFM1/M), permit directing the light through the objective as well as filtering the fluorescence signal. Measurements are performed with an Infinity Photo-Optical IF-3 objective lens of $M = 1\times$ magnification. Droplet impact images from bottom and side views are taken by a 12-bit, 2048×1952 pixels high-speed CMOS camera (Phantom T1340, Vision Research). The impact is recorded at a frame rate of 6200 fps and a resolution of 806× 806 pixels and 512×320 pixels for the bottom and side view, respectively. With these optical settings, the field of view spans 11.5×11.5 mm^2 for the bottom images and 19.46× 12.167 mm^2 for the side view. Additionally, the LIF apparatus can be traversed in three directions in steps of 1.25 µm enabling the adjustment of its position for image recording.

Rhodamine B dye (Carl Roth) is elected as fluorescent dye in the experiments. It has an absorption maximum at around 550 nm and emission maximum at 590 nm. The selection of rhodamine B as a label over rhodamine 6 G and fluorescein has been made due to its various advantages as concentration tracer as stated by Arcoumanis et al. (1990). As the signal intensity of rhodamine B is higher than that of rhodamine 6 G (Seno et al. 2001), it allows to detect lower concentrations and reconstruct smaller film thicknesses.

The disadvantage of using rhodamine B as fluorescent dye is its influence on the surface tension of water depending on its concentration (Seno et al. 2001). However, this has been taken into account in the present study as will be explained in Sect.. 5.1.

Table 1 Water properties and impact parameters. Droplet diameter is $D = 2.225 \pm 0.025$ mm

Parameters and fluid properties	Value
Kinematic viscosity ν (mm^2/s)	1.004
Density ρ (kg/m^3)	997
Surface tension σ (kg/s^2)	0.0723
Film thickness h (µm)	200; 500; 800
Dimensionless thickness δ (–)	0.09; 0.22; 0.36
Impact velocity U (m/s)	1.32
Reynolds number Re (–)	2967
Weber number We (–)	54

3 Method and calibration procedure

In order to determine the concentration distribution during the impact, it is necessary to establish a calibration technique that takes into consideration all the input parameters influencing the fluorescent signal. Let I_f be the intensity of the fluorescent signal. It can be expressed by the following equation (Guilbault 1973):

$$I_f = AI_0\Phi\epsilon LC, \tag{1}$$

where I_0 is the excitation light intensity, Φ is the fluorescence quantum yield, ϵ is the molar absorptivity, C is the dye concentration, and L is the depth of the lighted volume, which is the local thickness in this case. A is the fraction of the available light collected, because in reality not all the fluorescent light emitted is collected by the sensor.

The fluorescence response described in equation (1) is considered linear with respect to concentration. In fact, Arcoumanis et al. (1990) showed that this occurs for concentrations below 0.08 mg/L. The quantities of rhodamine B used during the calibration and experiments deliver concentrations ranging between 1 and 48 mg/L equivalent to 2×10^{-6}mol/L and 1×10^{-4} mol/L, respectively. The mol/L (M) unit will be used in the remainder of this paper. Moreover, the fluorescence signal is no more linear when surpassing a certain thickness threshold. Wigger et al. (2016) have shown that the fluorescence response deviates from linearity once the product of thickness and dye concentration is larger than $LC > 5$ µmm/L. Since the product of thickness and concentration of the liquid films used in measurements exceed this value, a multidimensional calibration is performed to extract the correlation between the fluorescence intensity, film thickness and concentration in form of fitting coefficients. Additionally, the calibration is also taking into account the in-plane local position (x, y). The inclusion of the spatial coordinates removes any remaining influence of uneven light distribution on the measurements. The maximum concentration of 1×10^{-4}M is chosen during calibration to avoid the self-quenching of Rhodamine B in aqueous solutions which was observed for concentrations higher than 3×10^{-4}M by Arbeloa et al. (1989).

The multidimensional calibration, which will be referred to as TIC calibration (Thickness, Intensity, Concentration) in the remainder of this paper, is achieved by taking multiple images of a set of thin films with known thickness and concentration. For noise reduction, a median filter with a kernel 5px×5px is applied. Afterward, each image was split into 25 interrogation windows. For each area, a second-order

polynomial regression between the fluorescence signal intensity and the spatial coordinates is found and expressed as follows:

$$I_f(x,y) = \sum_{k,l=0}^{2} a_{kl} \cdot x^k \cdot y^l. \tag{2}$$

Splitting the images into multiple interrogation windows was deemed critical for ensuring accurate calibration. In fact, a polynomial regression was initially attempted using the complete image. However, this approach did not yield an adequate fit as shown in Fig. 2a. In order to overcome this limitation, images were partitioned into multiple areas. By segmenting the image, better fits for each individual window were achieved (Fig. 2b), thereby enabling a more precise calibration. The number of interrogation windows was incrementally increased until the optimal fit was obtained.

The coefficients a_{kl} from all the images, which are a function of the dye concentration C and the film thickness h, are then regrouped and another polynomial regression is performed. This time, a third degree polynomial regression delivered an accurate prediction and is expressed in equation (3).

$$a_{kl}(C,h) = \sum_{i,j=0}^{3} b_{ij} \cdot C^i \cdot h^j. \tag{3}$$

Equation (2) can then be rewritten as follows:

$$I_f(C,h,x,y) = \sum_{k,l=0}^{2} \sum_{i,j=0}^{3} b_{ij} \cdot C^i \cdot h^j \cdot x^k \cdot y^l. \tag{4}$$

Concentrations can then be specifically obtained from equation (4) once all the other variables are known. In the following, validation measurements will be performed to determine how accurate and precise is the TIC calibration model.

4 Validation measurements

To validate the calibration approach described in Sect. 3, forty independent validation measurements for thin films of different thicknesses and dye concentrations were conducted. Each measurement was repeated five times to determine the precision of the technique. Throughout the validation Section, global as well as local errors and precisions of thickness and concentration reconstruction will be discussed.

4.1 Global error

An average across all pixels of the reconstructed film thickness and dye concentration will be calculated and compared with the CPS values and the known dye concentration, respectively. The global error is then calculated using equations (5) and (6):

$$\mathrm{Err_h} = \frac{|h_{\mathrm{avg}} - h_{\mathrm{CPS}}|}{h_{\mathrm{CPS}}} \times 100\%, \tag{5}$$

$$\mathrm{Err_C} = \frac{|C_{\mathrm{avg}} - C_r|}{C_r} \times 100\%, \tag{6}$$

where h_{avg} is the spatially averaged measured thickness, h_{CPS} is the thickness measured with CPS, C_{avg} is the spatially averaged measured concentration, and C_r is the known dye concentration. The reason behind determining the global error using the averaged measured thickness and concentration is

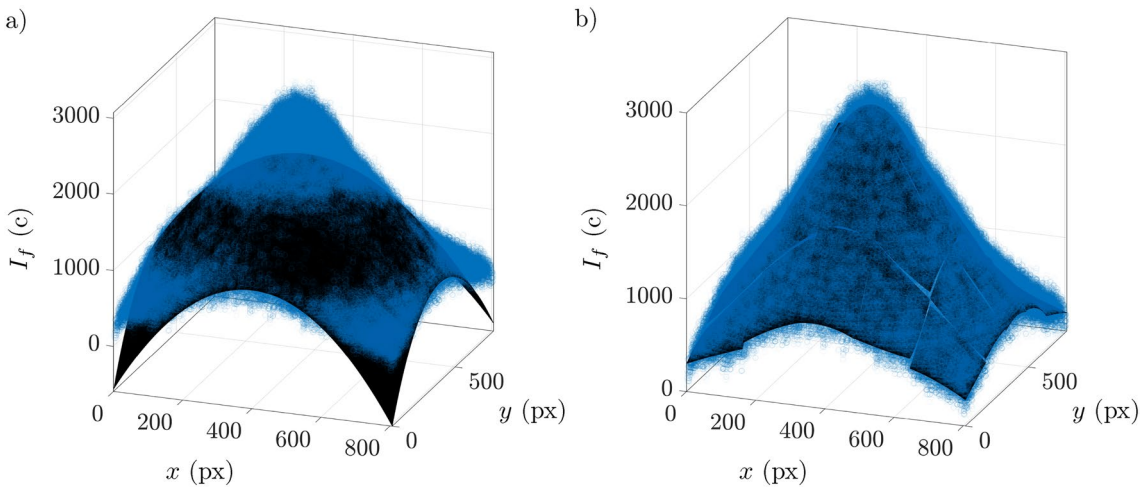

Fig. 2 Intensity fitting **a** without **b** with 25 interrogation windows. The blue circles represent the intensity values for each pixel, and the black curves represent the fit

to analyze the influence of initial parameters on the accuracy of the TIC calibration. Note that the accuracy and error are inversely related to each other.

A validation measurement is performed by taking 20 images of a thin film with a known thickness and dye concentration. Note that thin film measurements used for calibration are not used again for validation. The same noise reduction filter employed in the calibration is then applied to the set of images. After extracting the fluorescence intensity I_f of each pixel (x, y), equation (4) is used to obtain the local film thickness or the local dye concentration. In other words, if the wanted output is the liquid film thickness, the known initial dye concentration of the liquid film is used as input in the model, and vice versa. Let $h_i(x, y)$ be the reconstructed thickness of a certain pixel in the image i. The averaged thickness h_{avg} across all pixels and for all images is then calculated using all $h_i(x, y)$ and compared to the confocal sensor value as shown in Fig. 3a. The global error for all thickness reconstruction measurements is 3.83%. Identically, the average dye concentration is determined and is plotted in Fig. 3b, where the global error is 3.41%.

This measured error is highly influenced by the input parameters (Hidrovo and Hart 2001). For the validation measurements, the dye concentration as well as the film thickness is the only variables, and their influence is investigated and represented in Fig. 4. The global error for liquid film thickness reconstruction Err_h exhibits an inverse relationship with the reference dye concentration of the liquid film as highlighted by the regression curve in Fig. 4a. This increase in global error is due to a weak fluorescence signal for liquid films with low concentrations, resulting in decreasing signal-to-noise ratios. However, for extracting the film thickness variations during droplet impact, the rhodamine B concentration chosen is $C_0 = 8 \times 10^{-5}$M. This concentration grants not only a high signal to noise intensity for a wide range of liquid film thickness, but also a low reconstruction error. With respect to the film thickness influence, Fig. 4b displays a slight increasing behavior in the concentration reconstruction error Err_C as the liquid film thickness decreases. Analogously to liquid films with low concentrations, films with low thickness generate low signal to noise intensities which explain the decrease in accuracy. It can be noted that cases exhibiting high reconstruction error for thicknesses ranging between 600 µm and 1000 µm can be attributed to their low corresponding measured concentration as can be seen in Fig. 4b.

4.2 Local error

As mentioned in the beginning of this Section, a global error calculation is made to obtain a clear idea about the accuracy of the TIC calibration model within a certain range of dye concentrations and thicknesses. For evaluating the TIC calibration, the reconstruction error in each pixel, i.e., local error, is calculated using equations (5) and (6). In Fig. 5a,b, the mean 2D thickness and concentration reconstruction errors in each pixel of all validation measurements are presented. As can be seen, the error is less than 6% in most of the field of view. However, it increases radially to values up to 12% in the corner regions

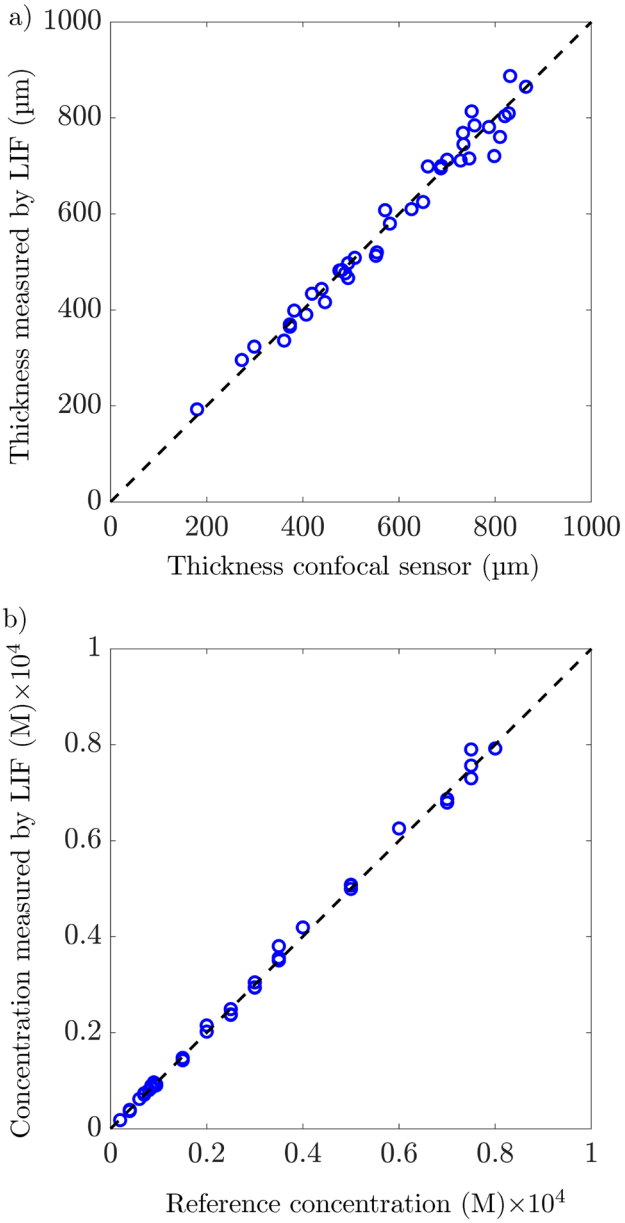

Fig. 3 **a** Comparison between LIF and confocal chromatic sensor measurements of the film thickness. **b** Comparison between LIF measurements and reference values of concentration

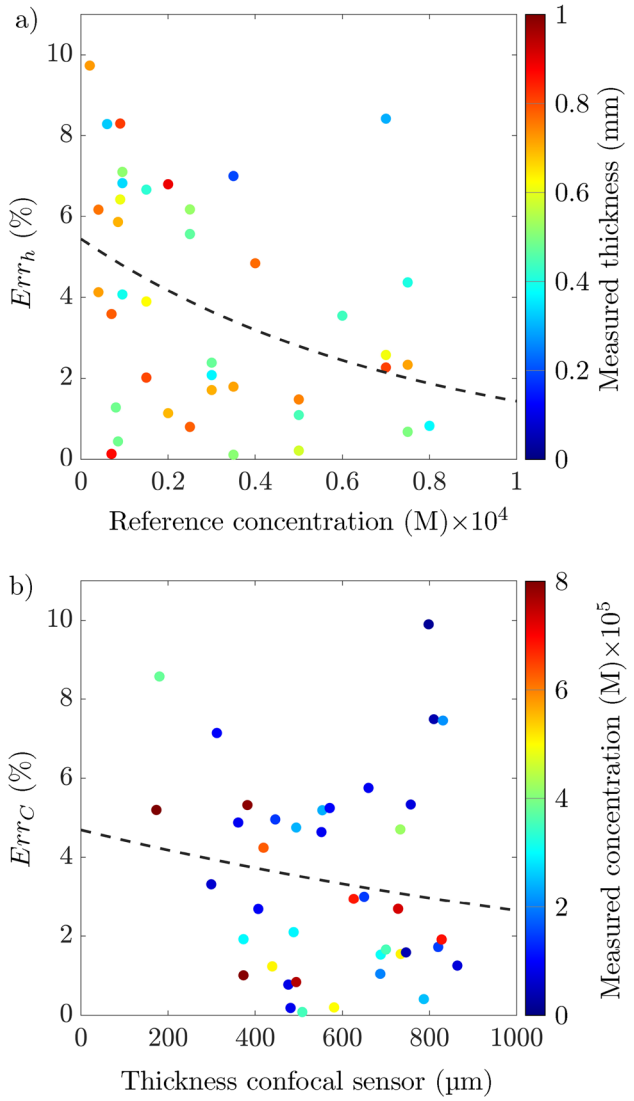

Fig. 4 **a** Influence of the reference dye concentration on the global thickness reconstruction error. Colors represent the film thickness measured by LIF. **b** Influence of the film thickness on the global concentration reconstruction error. Colors represent the concentration measured by LIF. The dashed lines represent regression fit of the data

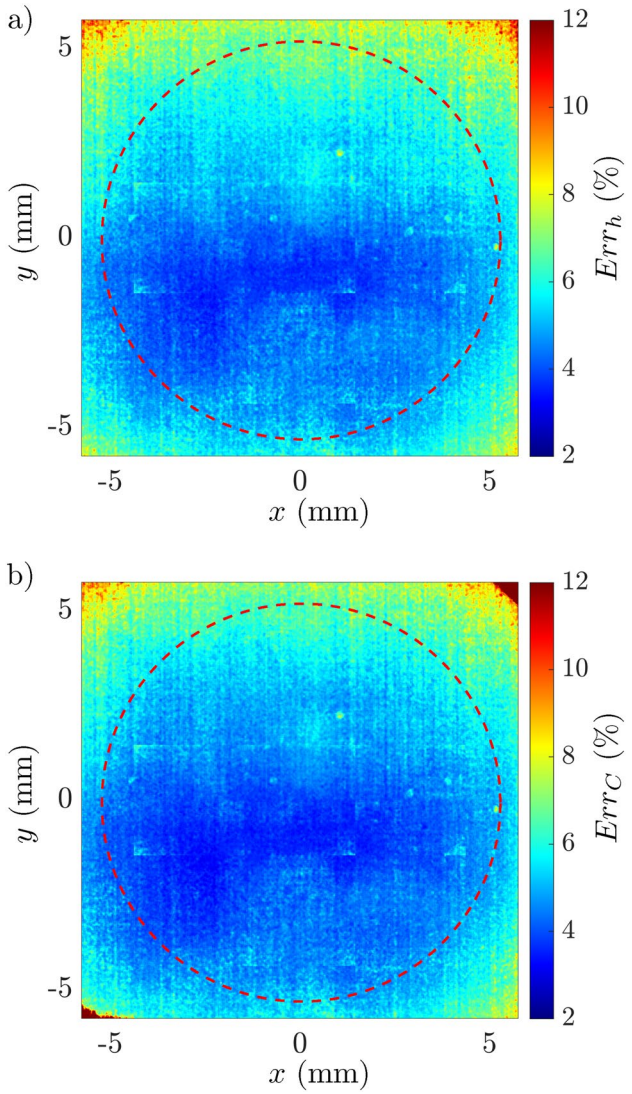

Fig. 5 Local error distribution using the TIC calibration for **a** film thickness reconstruction and **b** dye concentration reconstruction

of the field of view. This increase is due to the low signal to noise ratios near the corners of the image, notably for liquid films with low dye concentrations, which is caused by uneven illumination at the peripheries of the microscope (Likar et al. 2000). Known as vignetting, it causes a noticeable decrease in intensity toward the edges of the image, especially at low-magnification microscopy (Marty 2007). Furthermore, an observed small asymmetry between top and bottom halves in Fig. 5a may arise due the combination of the vignetting phenomenon and the optical system configuration leading to a small deviation between the center of the illumination and the center of the image. This latter leads to slightly higher thickness reconstruction errors for cases with low concentrations. As the impact and mixing occur in the center region of the image indicated with a dashed red circle in Fig. 5a, b, the corner regions will not affect the overall result accuracy.

The spatial average of the local error for all pixels for film thickness reconstruction is 4.82%, whereas it reaches 4.53% for concentration reconstruction. It was calculated by averaging the error values across all pixels in Fig. 5a, b. Note that this calculation procedure was also conducted by Li et al. (2019) for determining rhodamine B concentration in water inside an annular coolant system, where the average error across all pixels of 5.92%. In regard to the precision of the LIF method, the coefficient of variation (CV) is used to estimate the repeatability of the validation measurements. The CV of a single pixel is expressed by equation (7),

where σ_{sd} is the standard deviation and η is the mean of the 5 repeated measurements.

$$\mathrm{CV} = \frac{\sigma_{\mathrm{sd}}}{\eta} \times 100\%, \tag{7}$$

Using the equation above, the TIC calibration model delivers an average CV across all pixels of 3.62% for film thickness reconstruction and 3.63% for dye concentration reconstruction.

5 Drop impact on thin film

5.1 Experimental procedure

To investigate the mixing process of droplet impact onto thin liquid films, two complementary measurements are conducted. The first part, which will be further referred to as thickness measurements, is performed by labeling both the droplet and the film liquids with the same concentration of rhodamine B. During the impact, the fluorescence signal intensity variations are solely due to the film height variation. The chosen concentration is $C_0 = 8 \times 10^{-5}$M. Using the TIC calibration model, and given that the concentration is known and constant during the impact, instantaneous local film heights are determined. Subsequently, the second part of measurements is conducted, where only the film liquid is labeled by rhodamine B and has an initial concentration C_0. Spatially and temporally resolved concentrations are then obtained using the film height information from the preceding measurement. They will be referred to further as concentration measurements.

Within the scope of this work, only one impact velocity $U = 1.32$ m/s is investigated. As mentioned in Sect. 1, three film thicknesses are studied, where two films are representing the thin film category ($\delta = 0.22, \delta = 0.36$) and one film is representing the very thin film category ($\delta = 0.09$). The initial parameters chosen in this study lead to the deposition regime during the impact. As the mixing process is facilitated by turbulent eddy mixing, it is a stochastic process. Therefore, the impact experiments were performed five times for each case. Furthermore, the temperature during the impact was kept identical to calibration and validation measurements to 20°C. Figure 6 represents side and bottom view images of the impact for times up to $t = 40$ ms, where $t = 0$ ms corresponds to the impact instant. The choice of the investigated time duration after impact in this work is chosen to study the inertia driven convective mixing, only. Since the diffusion coefficient of rhodamine B is in the order of 10^{-10} m^2/s (Gendron et al. 2008), the mixing occurring during the elected period up to $t = 40$ ms after the impact is due to inertial forces. Note that the bottom view images shown in Fig. 6 are raw images before image processing.

Figure 6a,b shows droplet impact on a very thin film of thickness $\delta = 0.09$. After the first contact of the droplet with the film, an increase in the signal intensity is observed, which is due to the thickness increase at the rim during the spreading ($t = 1.6$ ms). Additionally, the impact creates an expanding crater with a remaining film thickness much lower compared to the initial film thickness before droplet impact. Hence, a low fluorescence intensity is observed here. In this study, the crater is defined by the circular region bounded by a steep gradient in the intensity signal ($t = 1.6$ ms). After the lamella spreading (Fig. 6b, $t = 1.6$ ms and $t = 4.7$ ms), finger-like shaped fluorescence pattern starts forming (Fig. 6b, $t = 9$ ms and $t = 20$ ms) during the collapse of the lamella rim. This pattern can be clearly seen in Fig. 7 for $\delta = 0.09$ at $t = 9$ ms. These structures occur during the receding phase and they have similarities to the fingering pattern observed during droplet impact onto dry surfaces, as can be seen in Fig. 1 of Marmanis and Thoroddsen 1996 and Fig. 26 of Thoroddsen and Sakakibara (1998). When transitioning from the very thin film to the thin film regime, the dominating mixing dynamics changes significantly as shown in Fig. 6d, f. One apparent difference is a decrease of the mixing area with increased thickness. The same trend was also observed by Ersoy and Eslamian (2019). This behavior is linked to the influence of the wall on the compression of the droplet during the impact. After the initial impact, the droplet penetrates the liquid film forming a crater growing in depth until reaching the wall. The interaction with the latter leads into a redirection of the kinetic energy dissipation in radial direction. When the film is very thin, a redirection of kinetic energy in the radial direction takes place earlier. At $t = 9$ ms, instability-driven finger formation can also be observed for dimensionless film thicknesses of $\delta = 0.22$ and $\delta = 0.36$ (see Fig. 6d, f).

In the context of droplet impact dynamics, it has been observed that vortex rings are formed during impacts onto liquid surfaces (Cresswell and Morton 1995). Due to the high velocity gradient across the liquid–liquid interface shortly after the impact, azimuthal vorticity is induced which develops into a vortex ring (Lee et al. 2015). Additionally, depending on the Reynolds number of the impact, Lee et al. (2015) have demonstrated that the impact can generate not only one but up to four vortex rings. Specifically, for the case Re = 2967 and We = 54 studied in the present work, three vortex rings are generated during the impact of a droplet onto another liquid surface, as shown by Lee et al. (2015). This latter prompt an investigation into the underlying factors contributing to the observed instabilities and if they are attributed to vortex ring instability. Considering that the primary focus of this study revolves around thin liquid films, it is nonetheless important to conduct investigations

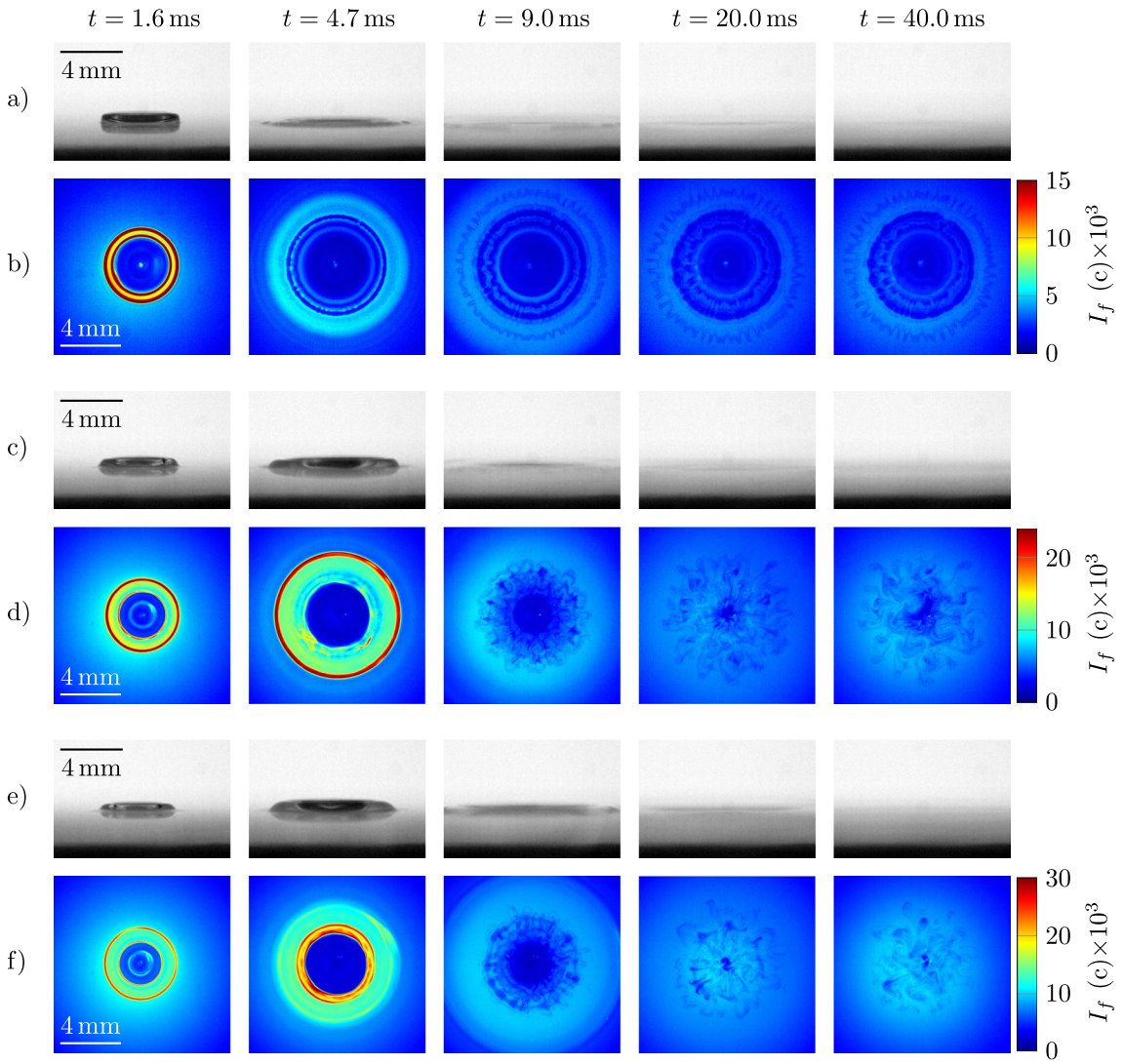

Fig. 6 Side and bottom view raw images of water droplet impact on fluorescent-labeled thin liquid film of different thicknesses for Re = 2967 and We = 54. **a**, **b** $\delta = 0.09$. **c**, **d** $\delta = 0.22$. **e**, **f** $\delta = 0.36$. The side view images are 19.46×12.16 mm^2, and the bottom view images are 11.5×11.5 mm^2. Colors represent the fluorescence signal intensity I_f

encompassing the two limit cases in regards of fluid film thickness to gain a comprehensive understanding of the factors causing the observed instabilities. Thus, two distinct cases are also examined: droplet impact on a dry substrate ($\delta = 0$) and into a pool ($\delta = 20$). To investigate the impact on a dry substrate, experiments using a rhodamine B dyed water droplet were conducted. The evolution of the impact is captured in Fig. 8a, revealing the spreading ($t = 1.6$ ms) and receding ($t = 14.3$ ms) of the droplet after the impact. At $t = 20$ ms, the droplet is already at rest and the signal intensity is notably higher in the center of the droplet compared to its edges. Since the droplet does not encounter any fluid film during the impact, there is no mixing. The dye concentration remains constant and the signal intensity difference can be attributed to the decrease in droplet height as it approaches the edges. Furthermore, the absence of finger-like shaped instabilities can also be observed in this case. Similar to the experiments conducted on the dry substrate using a dyed droplet, the ones for impacts into pool involve also dyeing the droplet with Rhodamine B instead of the pool itself. This choice comes from the limitations posed by the significant depth of the pool rendering the visualization of the mixing process through dyeing the entire pool unattainable. Figure 8b illustrates the various stages of droplet impact on pool ($\delta = 20$). At $t = 1.6$ ms, the droplet penetrates the pool, leading to the formation of vortex rings characterized by a pronounced intensity signal. A differentiation between each vortex ring at early stages from the bottom view is not feasible due to their overlapping. At $t = 14.3$ ms, azimuthal instabilities in form of loop-like structure can be spotted

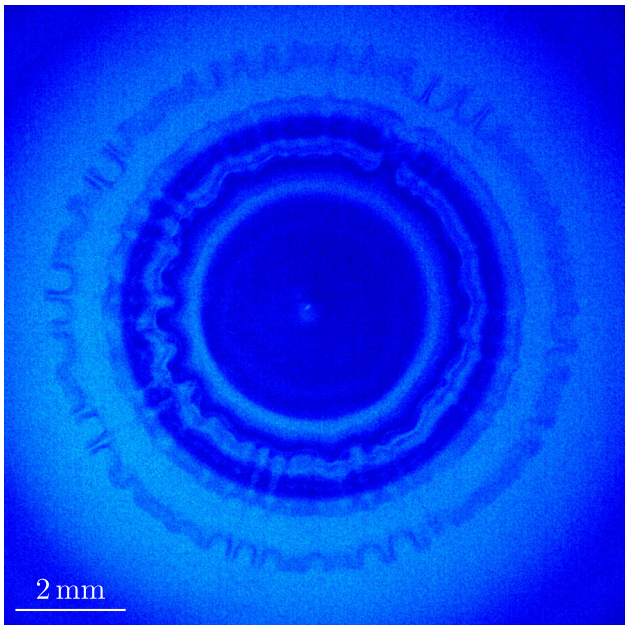

Fig. 7 Bottom view of water droplet impact on fluorescent-labeled thin liquid film of thickness $\delta = 0.09$ for Re = 2967 and We = 54 showcasing the finger-like patterns

in the region between the outer ring, indicated by the blue arrow, and the inner ring, indicated by the green arrow. Subsequently, the outer ring can be observed sinking down the pool at $t = 20$ ms and $t = 40$ ms. It may appear that the vortex ring is expanding, and however, it is important to note that the ring is not changing in size but rather going out of the range of focus of the camera, contributing to this visual effect. Despite the observed instabilities, both the inner and outer rings maintained their circular shape.

As mentioned previously, the impact in the studied case generates three vortex rings as shown by Lee et al. (2015). An interesting phenomenon observed during this process is the leapfrogging of two vortex rings, as can be seen in supplementary video 7 in the work of Lee et al. (2015). Leapfrogging occurs when two vortex rings, characterized by the same traveling direction and sense of rotation interact. As a consequence of mutual induction, the leading ring expands in size and moves at a slower pace, while the trailing ring contracts in size, accelerates and penetrates the leading ring. This cyclic process repeats itself until the two rings are merged, perpetuating the leapfrogging phenomenon (Shariff and Leonard 1992). According to Lim (1997b), the leapfrogging effect causes the azimuthal instabilities occurring during the passage between the two rings. Upon the subsequent merging of the two vortex rings, a portion of these instabilities remains behind in form of loop-like structure (Lim 1997a), as can be seen in Fig. 8b at $t = 14.3$ ms.

In the cases of droplet impacts on thin liquid films, the aforementioned vortex rings can undergo interactions with the wall that significantly affect their behavior. It is therefore plausible that the observed instabilities are also caused by the collision of the generated vortex rings with the wall. The evolution of the vortex ring during droplet impact onto thin film is presented in Fig. 9. Similar to previous cases, the presented impact involves a rhodamine B dyed water droplet and a pure water thin film of dimensionless

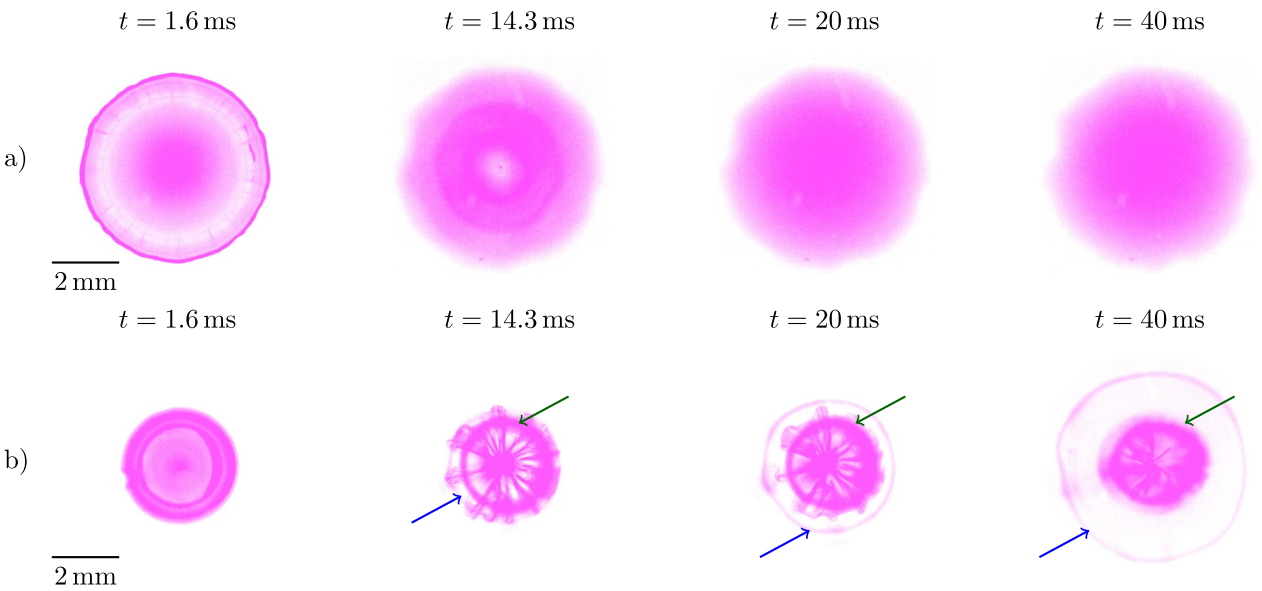

Fig. 8 Bottom view images of fluorescent-labeled droplet impact on **a** dry substrate $\delta = 0$ and **b** pure water pool thickness $\delta = 20$ for Re = 2967 and We = 54. The green arrows represent the inner ring, whereas the blue ones represent the outer ring

thickness $\delta = 0.36$. This latter configuration grants the possibility to observe vortex ring formation and decay during the spreading phase. After the creation of the vortex ring upon droplet impact, the ring approaches the wall, resulting in the formation of a boundary layer near the wall. Contrary to the behavior observed in the pool case, where the vortex ring maintained its size, in the thin film case, the vortex ring undergoes radial stretching upon collision with the wall. This can be observed during the transition from $t = 2.4$ ms in Fig. 9a to $t = 3.9$ ms in Fig. 9b. In contrast, for impact in pool, the vortex ring retained an inner diameter roughly equivalent to that of the droplet, as shown in Fig. 8b. According to Walker et al. (1987), the vortex ring stretching leads to the separation of the boundary layer under it from the wall. When the strength of this lift-off is sufficient, flow separation and the creation of a secondary vortex ring with an opposite-signed vorticity are initiated, which orbits the primary vortex ring (see Fig. 10) and leads into a rebound of the primary vortex ring from the wall as illustrated in the work of Chu et al. (1995) and Harris and Williamson (2012). At higher Reynolds numbers, the process of boundary layer separation also leads to the creation of a tertiary vortex ring (Cheng et al. 2010). The secondary vortex ring finally aligns inside the primary vortex ring and therefore can be distinguished in Fig. 9b at $t = 3.9$ ms through a light separation line. At a later stage, the secondary vortex ring exhibits azimuthal instabilities as shown in Fig. 9c at $t = 6.3$ ms. This behavior was also noticed by Cheng et al. (2010) in their numerical study of vortex ring impacting a flat wall. Furthermore, it is noteworthy that impacts on thin films exhibit a distinct behavior compared to impacts on a pool. Particularly, the outer ring for thin film cases

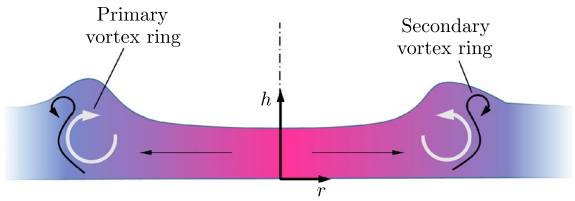

Fig. 10 Sketch of the counter-rotating primary and secondary vortex rings after droplet impact onto thin liquid film

undergoes instability resulting in figure-like patterns (see Figs. 7 and 9d), as opposed to the pool case. The presence of these patterns primarily arises from the instability induced by the interaction with the wall.

A combination of two different types of instabilities is responsible for vortex rings instability (Archer et al. 2010). Long-wavelength perturbations, also known as the Crow instability (Crow 1970), govern the vortex–wall interaction dynamics at low Reynolds number $\mathrm{Re}_\Gamma = \frac{\Gamma}{\nu}$, where Γ is the total circulation of the vortex ring. At higher Reynolds numbers, the Tsai–Widnall–Moore–Saffman (TWMS) instability, also referred to as elliptical instability (Tsai and Widnall 1976; Moore and Saffman 1975), dominates the vortex ring instability dynamics leading into short-wavelength perturbations and also causing the disintegration of the vortex ring into a turbulent cloud as can be seen in Fig. 9d. The dominance of the elliptical instability can also be observed in the formation of turbulent clouds at $t = 20$ ms for dimensionless thicknesses $\delta = 0.22$ and 0.36, as depicted in Fig. 6d, f. For $\delta = 0.09$, on the other hand, the lack of turbulent cloud is noticeable. Hence, the fluid film thickness has an influence

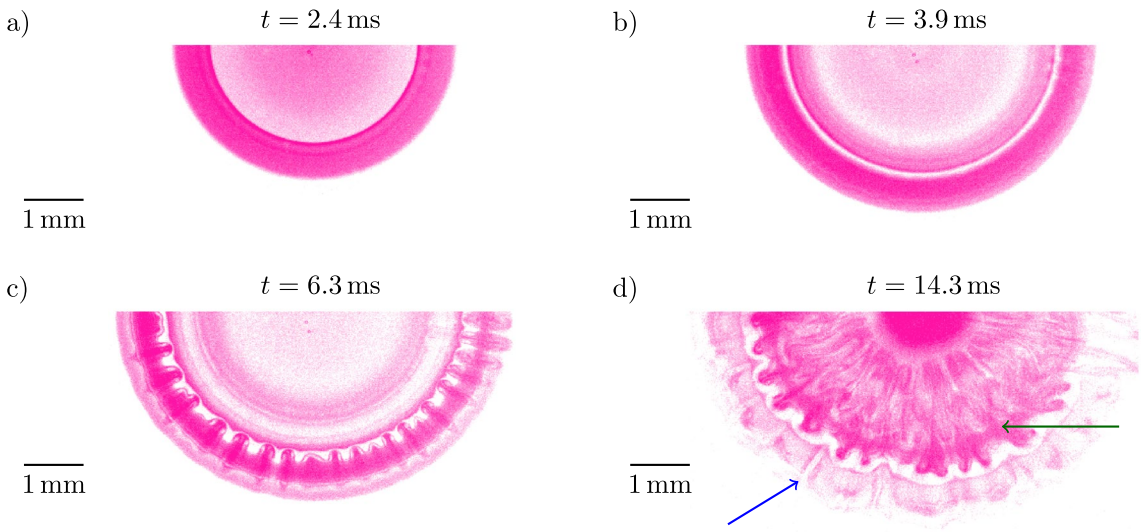

Fig. 9 Bottom view images of fluorescent-labeled droplet impact on pure water thin liquid film of thickness $\delta = 0.36$ for Re = 2967 and We = 54 illustrating vortex ring instabilities. The green arrow represents the inner vortex ring, whereas the blue one represents the outer vortex ring

on the vortex ring instability. Hence, the influence of the fluid film thickness on the vortex ring instability.

These two kinds of instabilities (long- and short-wavelength) were observed in both experimental (Walker et al. 1987; Leweke and Williamson 1998; Harris and Williamson 2012; McKeown et al. 2020) and numerical (Swearingen et al. 1995; Archer et al. 2010; Cheng et al. 2010; Mishra et al. 2021) studies for vortex ring interaction with a wall, however, investigations of vortex ring interactions in thin liquid films during droplet impact have not been studied in detail up to date. Wilkens et al. (2013) were the first ones to investigate vortex ring formation during droplet impact onto shallow pool, where they hypothesized that the observed waves are associated with the Crow instability. However, it is important to note that their investigation has primarily emphasized the examination of the vortex ring diameter resulting from impact on shallow pools rather than its instability. In contrast, the present study focuses on understanding the convective mixing process and the underlying mechanisms influencing it for droplet impacts onto very thin and thin films.

Figure 11a,b shows the case where both the droplet and the film liquids are labeled with rhodamine B for $\delta = 0.22$. In this way, the film thickness can be evaluated from the fluorescence signal. Therefore, the fluorescence signal intensity is higher for film thickness measurements compared to concentration measurements (Fig. 6d). The side view images are identical to the cases where only the liquid film is labeled with dye (Fig. 6c). One disadvantage of the LIF method, which was also mentioned by Hann et al. (2016), is the huge increase of the signal intensity in areas with larger slopes due to total reflection in the water–air interface, as can be seen at early impact times in Figs. 6 and 11. This effect does not allow for the observation of the ring structures forming earlier (see Fig. 9). Therefore, the investigation of mixing is started when this effect is avoided, thus when the wave amplitude is small compared to the wavelength.

As stated before in Sect. 2, rhodamine B impacts the surface tension of the liquid depending on the used amount for labeling. Hence, an examination into the influence of the used concentration of rhodamine B, $C_0 = 8 \times 10^{-5}$M on the mixing physics will be conducted. For this purpose, droplet impact on two films of the same thickness $\delta = 0.22$ and different dye concentrations is studied. Surface tension measurements were conducted using a tensiometer (DCAT 25 dataphysics-instruments) and surface tensions were measured by a Wilhelmy Plate tensiometer (DCAT 25 dataphysics-instruments). These are 65.34 ± 0.24 mN/m and 69.95 ± 0.11 mN/m for concentrations 8×10^{-5}M and 5×10^{-6}M, respectively. These values are in good agreement with Seno et al. (2001). Figure 12a, b represents the impact for both concentrations. The images were showed in grayscale as they are better visible in this way. Moreover, the LED used for side view recording is also illuminating the film for $C = 5 \times 10^{-6}$M to improve visibility. Hence, there occurs a reflection spot in Fig. 12b at $t = 9$ ms which does not exist for Fig. 12a. Additionally, due to the side illumination, the structures inside the crater are also visible. The vortex-driven mixing remains present in both cases and no apparent difference exists. As shown Fig. 6 in the work of Che and Matar (2017), surface tension effects due to surfactants tend to dampen the instabilities by virtue of their interfacial rigidifying effect (Constante-Amores et al. 2021) which leads into a circular shape of mixing instead of a decomposition of the vortex ring into a turbulent cloud. Therefore, for the chosen initial concentration $C_0 = 8 \times 10^{-5}$M no effect on the mixing process could be measured.

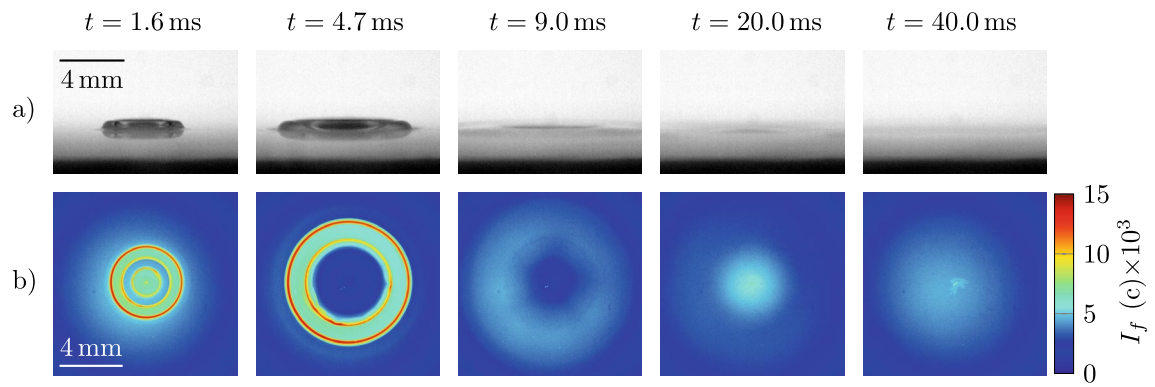

Fig. 11 Side and bottom view raw images of fluorescent-labeled droplet impact on fluorescent-labeled thin liquid film of thickness $\delta = 0.22$ for Re = 2967 and We = 54. The side view images in **a** are 19.46×12.16 mm^2 and the bottom view images in **b** are 11.5×11.5 mm^2. Colors represent the fluorescence signal intensity I_f

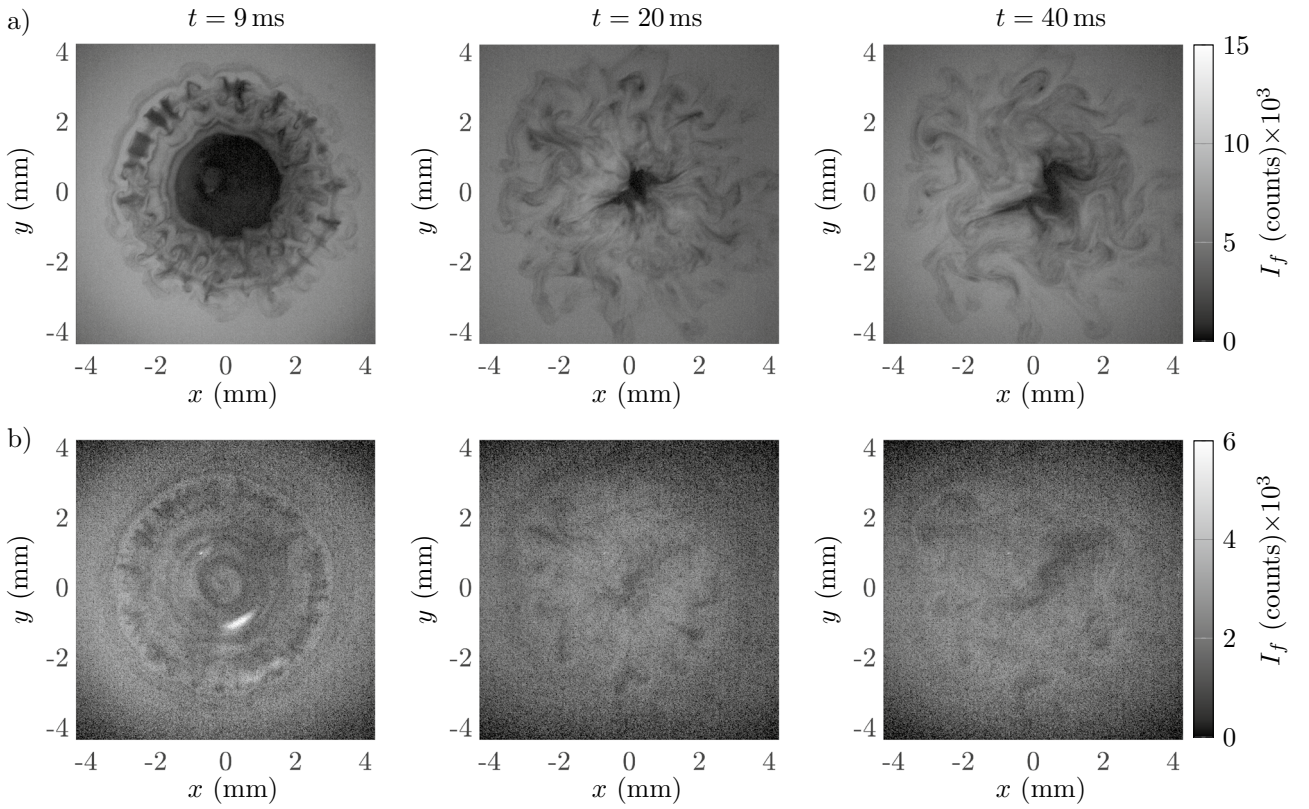

Fig. 12 Bottom view images of droplet impact on thin liquid film of thickness $\delta = 0.22$ for two different dye concentrations. **a** $C = 8 \times 10^{-5}$M and **b** $C = 5 \times 10^{-6}$M

5.2 Thickness measurements

In Fig. 13, the 2D local thickness of the film during the impact is presented. The x and y positions as well as the film height h_m are normalized by the droplet diameter D. One key aspect observed here is the rotational symmetry of the film thickness evolution during impact. This feature is used later on to separate fluorescence signal emanating from local thickness values and those purely related to concentration variations.

For certain time instances of the impact, the mean radial thickness profile is deducted from the 2D surface profiles by averaging the thicknesses corresponding to the same radial position r. This information is then used for the TIC calibration model. Radial dimensionless thickness profiles for $\delta = 0.09$ and $\delta = 0.22$ at $t_\mathrm{mix} = 3.7$ ms are plotted in Fig. 14a. The plotted values are the averaged reconstructed thicknesses in circumferential direction over all repeated measurements at fixed radial positions, where the error bars indicate the standard deviations. Due to the small standard deviations and smooth profile evolution also, slight height variations are detected providing a good picture of wave dynamics after impact. The precision of the radial thickness reconstruction depends on the local reconstruction accuracy itself but also on the repeatability of all five repeated measurements. Similarly to Sect. 4, equation (8), representing the coefficient of variation, is applied to quantify the radial thickness reconstruction precision.

$$\mathrm{CV}(r,t) = \frac{\sqrt{\frac{1}{n(r)-1}\sum_{i(r)}\left[h_{\mathrm{m}_i}(r,t) - \frac{1}{n(r)}\sum_{i(r)} h_{\mathrm{m}_i}(r,t)\right]^2}}{\frac{1}{n(r)}\sum_{i(r)} h_{\mathrm{m}_i}(r,t)}, \quad (8)$$

Here, $n(r)$ denotes the sample size for a given radius r, $h_{\mathrm{m}_i}(r,t)$ the measured thickness for a given radius at a given time and $i(r)$ represent the index of the the element in the sample. The spatial and temporal average of the coefficient of variation is then calculated by taking the average of CV values at each individual radius and time. For a single measurement, this average equals 3.51%, 3.62% and 4.72% for $\delta = 0.36$, $\delta = 0.22$ and $\delta = 0.09$, respectively. To account for the repeatability of the measurements, the average of CV is now calculated by including all 5 repeated measurements. The resulting CV averages are 5.47%, 5.27% and 6.67% for $\delta = 0.36$, $\delta = 0.22$ and $\delta = 0.09$, respectively. The small increase in the standard error with smaller thicknesses

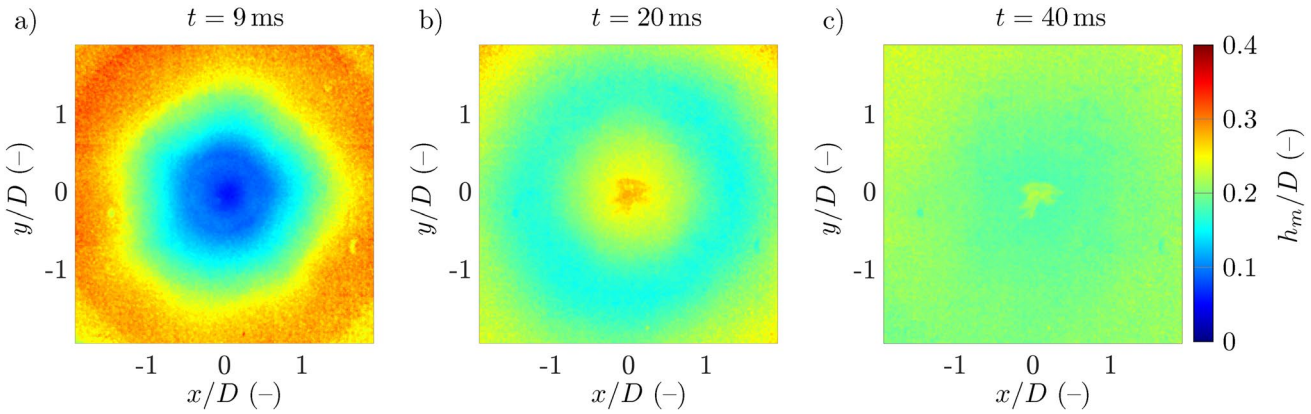

Fig. 13 2D film height reconstruction for $\delta = 0.22$ at different time instances after droplet impact **a** $t = 9$ ms; **b** $t = 20$ ms and **c** $t = 40$ ms. Colors represent film height normalized by droplet diameter

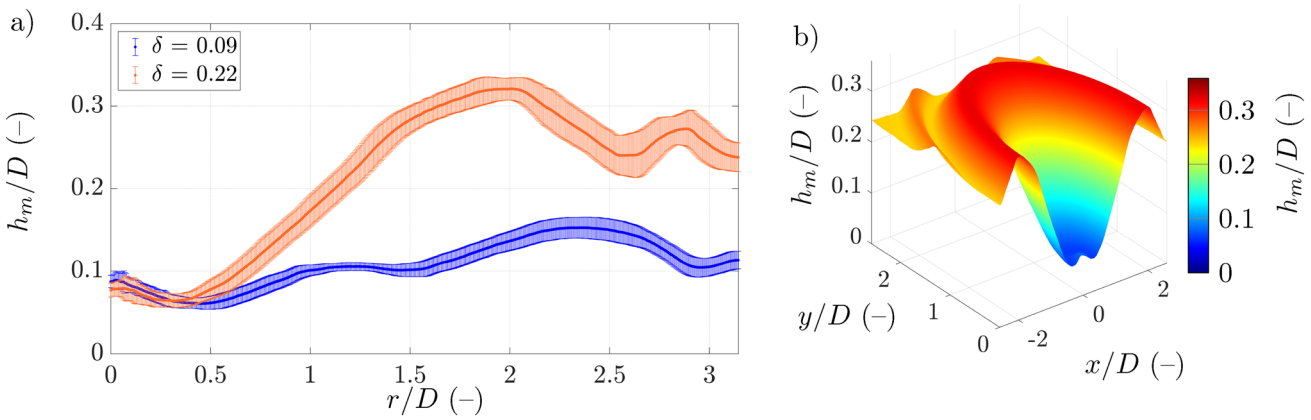

Fig. 14 **a** radial film height reconstruction showing the profile of the film during the impact at $t = 9$ ms for the cases $\delta = 0.09$ and $\delta = 0.22$. **b** 3D film height reconstruction for the case $\delta = 0.22$. The colors represent the film height normalized by droplet diameter

originates from a decreased intensity signal as explained in more detail in Sect. 4.

For a better visualization, the characteristic 3D surface shape of the impact can also be generated by performing a surface of revolution from the radial thickness graphs, as shown in Fig. 14b. The power of the LIF technique is its ability to detect other features happening during the impact such as propagation of surface waves, as shown in the left corner of the 3D reconstruction. Besides propagating capillary waves, a characteristic feature is the collection of liquid in the center of the crater at $t = 9$ ms (see Fig. 14b). It is assumed that this is a result of decay of the crater due to surface tension, thus an induced backflow toward the crater's center.

In the following, the averaged radial film thickness is used to derive radially resolved concentration profiles during the droplet impact.

5.3 Concentration distribution

A combination of TIC calibration model and the extracted local film height variations delivers the 2D dye concentration distribution during the impact as shown in Fig. 15. The initial dye concentration is $C_0 = 8 \times 10^{-5}$M which represents the maximum value in the colorbar. The mixing of the liquid film with pure water leads into a decrease of the local concentration. The established LIF method allows to determine the exact amount of liquid mixed and whether the mixing is homogeneous or not, as will be discussed in the following.

A first observation of the 2D distribution in Fig. 15a is the formation of finger-like instabilities of lower dye concentration. These originates from vortex ring instabilities, as discussed in Sect. 5.1, where an entrapment zone is generated. As the depth averaged concentration displays, stronger concentration gradients in radial direction are observed in the back and front edge of the vortex ring. This can also be seen at $t = 20$ ms in Fig. 15b. Note that the concentration

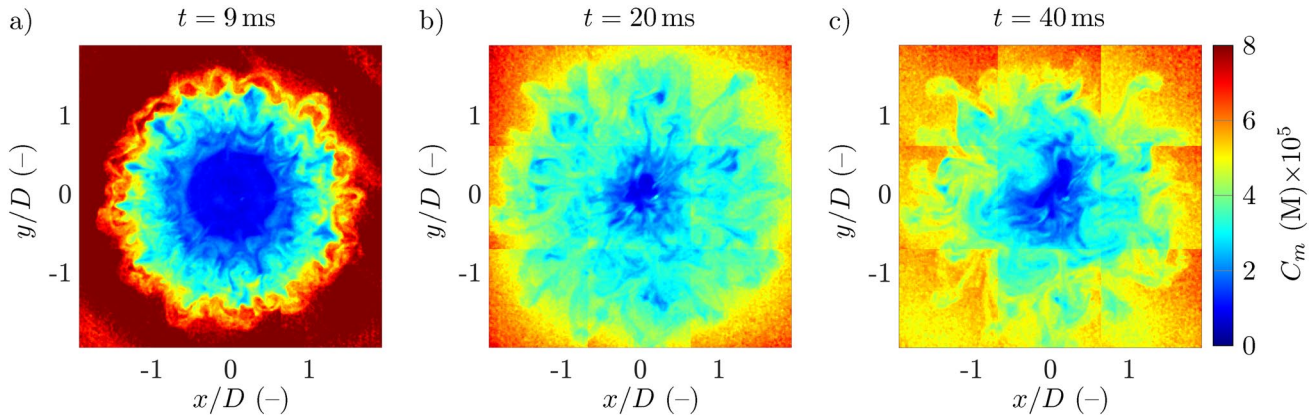

Fig. 15 2D dye concentration reconstruction for $\delta = 0.22$ at different time instances after droplet impact **a** $t = 9$ ms; **b** $t = 20$ ms and **c** $t = 40$ ms. The initial film concentration is $C_0 = 8 \times 10^{-5}$M mixing with a liquid drop of pure water $C_m = 0$M

jumps along the interrogation window edges shown in Fig. 15b, c result from the calibration procedure described in Sect. 3. These jumps are attributed to the small discontinuity between each fit at the boundaries of the interrogation windows as can be seen in Fig. 2b. Furthermore, the accumulated error from the radial thickness measurements may also affect the continuity between the interrogation windows and contribute into these slight concentration gradients along the edges.

The radial concentration profile is derived in analogy to the radial thickness profile from averaging in circumferential direction. Results are plotted in Fig. 16a for a selected measurement of film thickness $\delta = 0.22$ at $t = 9$ ms and $t = 40$ ms. Note that the measured concentration C_{m} and the radius r are normalized by C_0 and D. Consistent with the observation of stronger concentration gradient in the back and front edge of the vortex ring described earlier, the radial concentration plot at $t = 9$ ms (Fig. 16a) also exhibits a similar pattern. As time progresses up to $t = 40$ ms, these gradients tends to gradually flatten out, leading into more uniform distribution of concentration. This can be attributed to the disintegration of the vortex ring into a turbulent cloud, which enhances mixing and leads into a more even distribution of concentration.

Next, the radial concentration of repeated measurements each will be compared for $\delta = 0.22$. As mentioned before, the mixing process is turbulent, with certain characteristic coherent vortical structures such as the vortex ring. The chaotic behavior of the vortex ring decay leads to variations in the local concentration distribution as shown in Figs. 6d and 12a at $t = 40$ ms. However, the radial concentration distribution at $t = 40$ ms is very similar for all repeated measurements as presented in Fig. 16b. Differences are mainly visible near the impact center between $r/D = 0$ and $r/D = 0.5$. Here, the concentration is also normalized by C_0. This is due to the fact that the drop liquid, remaining at the center of the

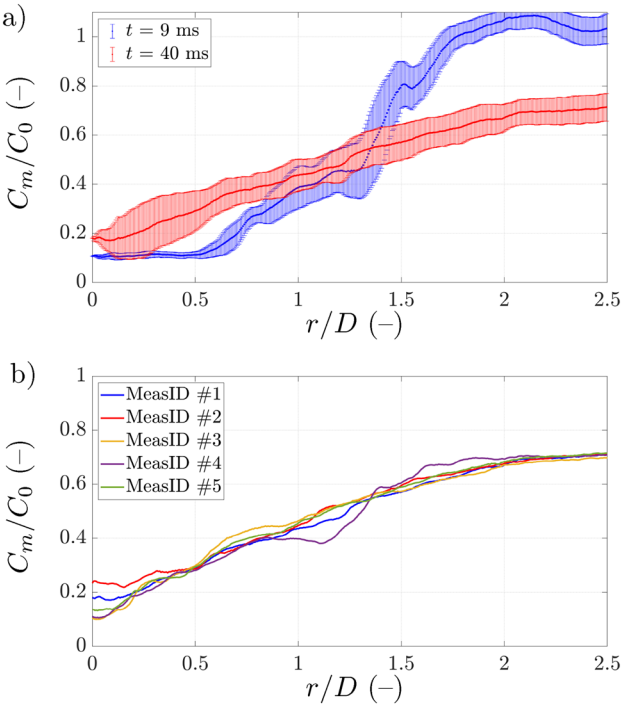

Fig. 16 **a** radial dye concentration graph for the case $\delta = 0.22$ at $t = 9$ ms and $t = 40$ ms. **b** radial dye concentration graph of all the measurements for the case $\delta = 0.22$ at $t = 40$ ms

impact after the receding phase, encounters deformations caused by the turbulent disintegration of the vortex ring. As a result, the liquid present in the center undergoes different displacement in each measurement, thus the observed differences in radial concentration distributions near the central region.

In the context of mixing performance, the coefficient of variation (CV_C) can be used as an indicator of the degree of

mixing or homogeneity in a system (Gandhi et al. 2011). It is expressed by the following equation:

$$\mathrm{CV_C}(t) = \frac{\sqrt{\frac{1}{n-1}\sum_{x,y}\left[C_\mathrm{m}(x,y,t) - \frac{1}{n}\sum_{x,y} C_\mathrm{m}(x,y,t)\right]^2}}{\frac{1}{n}\sum_{x,y} C_\mathrm{m}(x,y,t)}, \quad (9)$$

where n denotes the sample size defining the mixing area, $C_\mathrm{m}(x, y)$ the measured local concentration in the position (x,y) at a given time t. Note that the chosen mixing area differs in thickness, since this area increases with decreased thickness as mentioned in Sect. 5.1. Furthermore, the criteria determining the selection of the mixing area in the computation of CV_C are the maximum expansion of the vortex ring as well as the concentration gradient in the front edge of the ring.

A lower coefficient of variation indicates a more homogeneous distribution of the droplet liquid, suggesting a higher degree of mixing. Conversely, a higher CV_C indicates a less homogeneous distribution, implying poorer mixing performance. Figure 17a represents the temporal variations of CV_C for all the cases, where the error bars indicate the standard deviations of the repeated measurements. For the thickness $\delta = 0.09$, the CV_C decreases and reaches rapidly a steady value, indicating a short convective mixing period followed by diffusion. In contrast, for thicknesses $\delta = 0.22$ and $\delta = 0.36$, the CV_C continues to decrease over a longer period due to convection-driven mixing induced by the disintegration of the vortex ring. Notably, the coefficient of variation for $\delta = 0.36$ decreases even more, indicating a stronger convective mixing effect associated with thicker liquid layers. These observations suggest that the film thickness significantly affects the mixing behavior, with thicker films exhibiting prolonged convection-driven mixing. In Fig. 17b, radial concentration distributions for the three thickness at $t = 20$ ms are compared. The thinnest film, i.e., $\delta = 0.09$, exhibits a distinct pattern compared to the other thicknesses, characterized by sharp concentration gradients. In addition, the initial concentration increase in radial direction is followed by a decrease and then another increase. For $\delta = 0.09$, the instabilities occurring during the impact are not strong enough to lead into a vortex ring decay (see Fig. 6b), resulting into a clear primary (low concentration) and secondary (high concentration) vortex rings, which explains the wave-like sequence.

Moreover, a slight increase in CV_C values can be seen at $t = 22.5$ ms for $\delta = 0.22$ and $\delta = 0.36$ in Fig. 17a. This latter is attributed to the spreading of the small jet (see Fig. 11 at $t = 20$ ms) after the receding phase, which predominantly consists of the droplet liquid. It can also be clearly observed in the corresponding videos that are available in supplementary material (Ennayar et al. 2023).

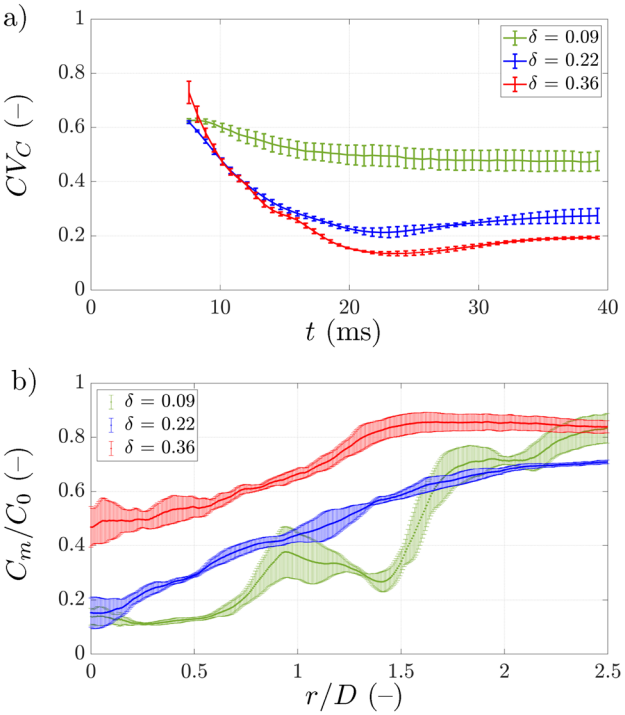

Fig. 17 **a)** The temporal variation of the coefficient of variation CV_C for the cases $\delta = 0.09$ (green) $\delta = 0.22$ (blue) and $\delta = 0.36$ (red). **b)** Radial concentration distribution for the cases $\delta = 0.09$ (green) $\delta = 0.22$ (blue) and $\delta = 0.36$ (red) at $t = 40$ ms

6 Conclusion

In the present work, a LIF-based measurement technique is developed to quantitatively investigate the mixing process during droplet impact on thin films of different thicknesses ($\delta = 0.09$, $\delta = 0.22$ and $\delta = 0.36$). First, a calibration procedure was developed enabling the extraction of local film thickness and dye concentration. Subsequently, the calibration model was validated through a series of measurements, in which the model delivered accurate results with concentration and thickness reconstruction errors of 4.53% and 4.82%, respectively, as well as precision errors of 3.62% and 3.63%, respectively. Measurements were then conducted in two steps, where the local film thicknesses during the impact were determined first and the 2D concentration was extracted from a subsequent repetition measurement utilizing the thickness measurements results. Furthermore, it was shown that the dye concentration $C_0 = 8 \times 10^{-5}$M used for labeling had no measurable influence on the mixing process.

For the first time, we observe wall-induced elliptical vortex ring instability during droplet impact onto thin liquid film. The vortex ring formed during a droplet impact onto a thin liquid film approaches the wall resulting in the

formation of a boundary layer and undergoing instabilities upon collision.

In our experiments, this instability leads to the disintegration of the vortex ring into a turbulent cloud. This observed instability is similar to the instability described by Cheng et al. (2010) for a vortex impacting a flat wall which is governed by the superposition of the Crow and the elliptical instability. In addition, significant differences were observed between the behavior of the vortex rings in droplet impact on a pool compared to impacts onto thin liquid films. In the pool case, the rings preserved their circular form and the inner ring maintained an inner diameter roughly equivalent to the droplet. On the other hand, in thin liquid film cases, the outer ring exhibited instabilities in form of finger-like patterns. Ultimately, a statistical analysis using the coefficient of variation was conducted to quantify the degree of mixing during the impact. The findings demonstrated that the vortex ring disintegration after droplet impact plays a key role on the mixing performance. Furthermore, slight increases of the film thickness within the thin film regime can lead to a transition from a sub- to a supercritical flow regime where the elliptical instability leads to flow interaction and vortex ring disintegration.

Author contributions HE contributed to investigation, methodology, data analysis and writing-original draft; PB was involved in methodology, data analysis, writing-review and editing; JH contributed to conceptualization, supervision, writing-review and editing, project administration and funding acquisition.

Funding Open Access funding enabled and organized by Projekt DEAL. This project is funded by the Deutsche Forschungsgemeinschaft (DFG, German Research Foundation) - project number 237267381 - TRR 150, sub-project A07. Philipp Brockmann was financially supported by the Deutsche Forschungsgemeinschaft (DFG, German Research Foundation)—Project Number 265191195—SFB 1194, subproject A03.

Data availability Supplementary material can be found in Ennayar et al. (2023). This contains all data plotted in figures, as well as the metadata of experiments. Recorded videos of droplet impacts, from which the images of figures are extracted, are also included.

Declarations

Conflict of interest The authors have no competing interests to declare that are relevant to the content of this article.

Ethical approval This declaration is not applicable.

References

Alonso M, Kay PJ, Bowen PJ, Gilchrist R, Sapsford S (2010) A laser induced fluorescence technique for quantifying transient liquid fuel films utilising total internal reflection. Exp Fluids 48(1):133–142

Andresen P, Strube G (1994) Laser induced fluorescence. In: Techniques and applications, optical measurements, pp 243–272

Arbeloa FL, Ojeda PR, Arbeloa IL (1989) Flourescence self-quenching of the molecular forms of rhodamine b in aqueous and ethanolic solutions. J Lumin 44(1–2):105–112

Archer P, Thomas T, Coleman G (2010) The instability of a vortex ring impinging on a free surface. J Fluid Mech 642:79–94

Arcoumanis C, McGuirk J, Palma J (1990) On the use of fluorescent dyes for concentration measurements in water flows. Exp Fluids 10(2):177–180

Berberović E, van Hinsberg NP, Jakirlić S, Roisman IV, Tropea C (2009) Drop impact onto a liquid layer of finite thickness: dynamics of the cavity evolution. Phys Rev E 79(3):036306

Breitenbach J, Roisman IV, Tropea C (2018) From drop impact physics to spray cooling models: a critical review. Exp Fluids 59(3):1–21

Che Z, Matar OK (2017) Impact of droplets on liquid films in the presence of surfactant. Langmuir 33(43):12140–12148

Chen N, Chen H, Amirfazli A (2017) Drop impact onto a thin film: miscibility effect. Phys Fluids 29(9):092106

Cheng M, Lou J, Luo L-S (2010) Numerical study of a vortex ring impacting a flat wall. J Fluid Mech 660:430–455

Chu C-C, Wang C-T, Chang C-C (1995) A vortex ring impinging on a solid plane surface-vortex structure and surface force. Phys Fluids 7(6):1391–1401

Constante-Amores C, Batchvarov A, Kahouadji L, Shin S, Chergui J, Juric D, Matar O (2021) Role of surfactant-induced Marangoni stresses in drop-interface coalescence. J Fluid Mech 925:A15

Cossali GE, Coghe A, Marengo M (1997) The impact of a single drop on a wetted solid surface. Exp Fluids 22(6):463–472

Cresswell R, Morton B (1995) Drop-formed vortex rings-the generation of vorticity. Phys Fluids 7(6):1363–1370

Crow SC (1970) Stability theory for a pair of trailing vortices. AIAA J 8(12):2172–2179

Demtröder W (2014) Laser spectroscopy 2. Experimental techniques. Springer, Berlin, p 5

Dossmann Y, Bourget B, Brouzet C, Dauxois T, Joubaud S, Odier P (2016) Mixing by internal waves quantified using combined piv/plif technique. Exp Fluids 57(8):1–12

Ennayar H, Brockmann P, Hussong J (2023) LIF-based quantification of the species transport during droplet impact onto thin liquid films. In: Supplementary Data. Zenodo. https://doi.org/10.5281/zenodo.7888556

Ersoy NE, Eslamian M (2019) Capillary surface wave formation and mixing of miscible liquids during droplet impact onto a liquid film. Phys Fluids 31(1):012107

Gandhi V, Roberts PJ, Stoesser T, Wright H, Kim J-H (2011) Uv reactor flow visualization and mixing quantification using three-dimensional laser-induced fluorescence. Water Res 45(13):3855–3862

Gendron P-O, Avaltroni F, Wilkinson K (2008) Diffusion coefficients of several rhodamine derivatives as determined by pulsed field gradient-nuclear magnetic resonance and fluorescence correlation spectroscopy. J Fluoresc 18(6):1093–1101

Geppert A. K. (2019). Experimental investigation of droplet wall-film interaction of binary systems
Guilbault GG (1973) Practical fluorescence: theory, methods and techniques. Dekker, New York
Hann DB, Cherdantsev AV, Mitchell A, McCarthy I, Hewakandamby BN, Simmons K (2016) A study of droplet impact on static films using the bb-lif technique. Exp Fluids 57(4):1–12
Harris D, Williamson C (2012) Instability of secondary vortices generated by a vortex pair in ground effect. J Fluid Mech 700:148–186
Haugland RP (1996) Handbook of fluorescent probes and research chemicals. Molecular Probes, Eugene, p 8
Hidrovo CH, Hart DP (2001) Emission reabsorption laser induced fluorescence (erlif) film thickness measurement. Meas Sci Technol 12(4):467
Israelachvili JN (2011) Intermolecular and surface forces. Academic press, Cambridge
Josserand C, Thoroddsen ST (2016) Drop impact on a solid surface. Annu Rev Fluid Mech 48(1):365–391
Khan T, Ersoy NE, Eslamian M (2020) Droplet impact on a wavy liquid film under multi-axis lateral vibrations. Exp Fluids 61(8):1–21
Kim H, Lee J, Kim T-H, Kim H-Y (2015) Spontaneous marangoni mixing of miscible liquids at a liquid-liquid-air contact line. Langmuir 31(31):8726–8731
Kim H, Muller K, Shardt O, Afkhami S, Stone HA (2017) Solutal marangoni flows of miscible liquids drive transport without surface contamination. Nat Phys 13(11):1105–1110
Kittel HM, Roisman IV, Tropea C (2018) Splash of a drop impacting onto a solid substrate wetted by a thin film of another liquid. Phys Rev Fluids 3(7):073601
Klyuzhin IS, Ienna F, Roeder B, Wexler A, Pollack GH (2010) Persisting water droplets on water surfaces. J Phys Chem B 114(44):14020–14027
Koochesfahani M, Dimotakis P (1985) Laser-induced fluorescence measurements of mixed fluid concentrationin a liquid plane shear layer. AIAA J 23(11):1700–1707
Kurniawan T, Tsai P-H, Chen S-S, Frakes DH, Chen C-C, Wang A-B (2022) Practical notes toward higher quality and more reliable experiments on drop and liquid surface interactions. Exp Fluids 63:1–27
Lee JS, Park SJ, Lee JH, Weon BM, Fezzaa K, Je JH (2015) Origin and dynamics of vortex rings in drop splashing. Nat Commun 6(1):8187
Leweke T, Williamson CH (1998) Cooperative elliptic instability of a vortex pair. J Fluid Mech 360:85–119
Lhuissier H, Sun C, Prosperetti A, Lohse D (2013) Drop fragmentation at impact onto a bath of an immiscible liquid. Phys Rev Lett 110(26):264503
Li X, Qi P, Zhao T, Qiao S, Tan S (2019) Lif study of temporal and spatial fluid mixing in an annular downcomer. Ann Nucl Energy 126:220–232
Li Y, Zheng Y, Lan Z, Xu W, Ma X (2017) The evolution of droplet impacting on thin liquid film at superhydrophilic surface. Appl Phys Lett 111(23):231601
Likar B, Maintz JA., Viergever, MA, Pernus, F. (2000) Retrospective shading correction based on entropy minimization. J Microsc 197(Pt 3):285–295
Lim T (1997) A note on the leapfrogging between two coaxial vortex rings at low reynolds numbers. Phys Fluids 9(1):239–241
Lim T (1997) On the role of kelvin-helmholtz-like instability in the formation of turbulent vortex rings. Fluid Dyn Res 21(1):47–56
Maliha M, Stumpf B, Beyer F, Kühnert M, Kubach H, Roisman I, Hussong J, Koch T (2022) Optical investigation on the interaction between a fuel-spray and an oil wetted wall with the focus on secondary droplets. Int J Eng Res 24(4):1578–1588
Marmanis H, Thoroddsen S (1996) Scaling of the fingering pattern of an impacting drop. Phys Fluids 8(6):1344–1346
Marty GD (2007) Blank-field correction for achieving a uniform white background in brightfield digital photomicrographs. Biotechniques 42(6):716–720
McKeown R, Ostilla-Mónico R, Pumir A, Brenner MP, Rubinstein SM (2020) Turbulence generation through an iterative cascade of the elliptical instability. Sci Adv 6(9):eaaz2717
Mishra A, Pumir A, Ostilla-Mónico R (2021) Instability and disintegration of vortex rings during head-on collisions and wall interactions. Phys Rev Fluids 6(10):104702
Moore DW, Saffman PG (1975) The instability of a straight vortex filament in a strain field. Proc R Soc Lond A Math Phys Sci 346(1646):413–425
Mundo C, Sommerfeld M, Tropea C (1995) Droplet-wall collisions: experimental studies of the deformation and breakup process. Int J Multiph Flow 21(2):151–173
Okawa T, Shiraishi T, Mori T (2006) Production of secondary drops during the single water drop impact onto a plane water surface. Exp Fluids 41(6):965–974
Oldenziel G, Delfos R, Westerweel J (2012) Measurements of liquid film thickness for a droplet at a two-fluid interface. Phys Fluids 24(2):022106
Owen, F. (1976). Simultaneous laser measurements of instantaneous velocity and concentration in turbulent mixing flows. In AGARD Appl. of Non-Intrusive Instr. in Fluid Flow Res. p 7 (SEE N77-11221 02-31)
Pan K-L, Law CK (2007) Dynamics of droplet-film collision. J Fluid Mech 587:1–22
Rioboo R, Bauthier C, Conti J, Voue M, De Coninck J (2003) Experimental investigation of splash and crown formation during single drop impact on wetted surfaces. Exp Fluids 35(6):648–652
Roisman IV, Horvat K, Tropea C (2006) Spray impact: rim transverse instability initiating fingering and splash, and description of a secondary spray. Phys Fluids 18(10):102104
Roisman IV, Tropea C (2002) Impact of a drop onto a wetted wall: description of crown formation and propagation. J Fluid Mech 472:373–397
Roisman IV, van Hinsberg NP, Tropea C (2008) Propagation of a kinematic instability in a liquid layer: capillary and gravity effects. Phys Rev E 77(4):046305
Schulz F, Samenfink W, Schmidt J, Beyrau F (2016) Systematic lif fuel wall film investigation. Fuel 172:284–292
Seno K, Ishioka T, Harata A, Hatano Y (2001) Photoionization of rhodamine dyes adsorbed at the aqueous solution surfaces investigated by synchrotron radiation. Anal Sci Suppl 17icas:i1177–i1179
Shaikh S, Toyofuku G, Hoang R, Marston J (2018) Immiscible impact dynamics of droplets onto millimetric films. Exp Fluids 59(1):1–12
Shariff K, Leonard A (1992) Vortex rings. Annu Rev Fluid Mech 24(1):235–279
Swearingen J, Crouch J, Handler R (1995) Dynamics and stability of a vortex ring impacting a solid boundary. J Fluid Mech 297:1–28
Thoroddsen S, Sakakibara J (1998) Evolution of the fingering pattern of an impacting drop. Phys Fluids 10(6):1359–1374
Thoroddsen ST, Takehara K, Etoh T (2012) Micro-splashing by drop impacts. J Fluid Mech 706:560–570
Tropea C, Marengo M (1999) The impact of drops on walls and films. Multiph Sci Technol 11(1):19–36
Tropea C, Roisman IV (2000) Modeling of spray impact on solid surfaces. At sprays 10(3–5):387–408
Tsai C-Y, Widnall SE (1976) The stability of short waves on a straight vortex filament in a weak externally imposed strain field. J Fluid Mech 73(4):721–733

Van Hinsberg NP, Budakli M, Göhler S, Berberović E, Roisman IV, Gambaryan-Roisman T, Tropea C, Stephan P (2010) Dynamics of the cavity and the surface film for impingements of single drops on liquid films of various thicknesses. J Colloid Interface Sci 350(1):336–343

Wal RLV, Berger GM, Mozes SD (2006) The splash/non-splash boundary upon a dry surface and thin fluid film. Exp Fluids 40(1):53–59

Walker D (1987) A fluorescence technique for measurement of concentration in mixing liquids. J Phys E Sci Instrum 20(2):217

Walker J, Smith CR, Cerra A, Doligalski T (1987) The impact of a vortex ring on a wall. J Fluid Mech 181:99–140

Wang A-B, Chen C-C (2000) Splashing impact of a single drop onto very thin liquid films. Phys Fluids 12(9):2155–2158

Wigger S, Füßer H-J, Fuhrmann D, Schulz C, Kaiser SA (2016) Quantitative two-dimensional measurement of oil-film thickness by laser-induced fluorescence in a piston-ring model experiment. Appl Opt 55(2):269–279

Wilkens A, Auerbach D, van Heijst G (2013) Vortex ring generation during drop impact into a shallow pool. arXiv preprint arXiv:1305.0403

Yarin AL et al (2006) Drop impact dynamics: splashing, spreading, receding, bouncing. Annu Rev Fluid Mech 38(1):159–192